Surfaces and Interfaces 26 (2021) 101367

Contents lists available at ScienceDirect

Surfaces and Interfaces

journal homepage: www.sciencedirect.com/journal/surfaces-and-interfaces

Fabrication of electrospun nanofiber composite of g-C_3N_4 and Au nanoparticles as plasmonic photocatalyst

Dipendu Saha [a,*], Pasquale Gismondi [a], Kurt W. Kolasinski [b], Samantha L. Shumlas [b], Sylvie Rangan [c], Babak Eslami [d], Amy McConnell [a], TaeVaughn Bui [a], Kayla Cunfer [a]

[a] Chemical Engineering Department, Widener University, 1 University Place, Chester, PA 19013, United States
[b] Department of Chemistry, West Chester University, West Chester, PA 19383, United States
[c] Department of Physics and Astronomy and Laboratory for Surface Modification, Rutgers University, 136 Frelinghuysen Road, Piscataway, New Jersey 08854, United States
[d] Mechanical Engineering Department, Widener University, 1 University Place, Chester, PA 19013, United States

ARTICLE INFO

Keywords:
Photocatalyst
Electrospinning
Nanofiber
Gold nanoparticle
Plasmonic

ABSTRACT

In this research, we have fabricated a composite nanofiber mat of plasmonic photocatalyst consisting of g-C_3N_4, gold nanoparticles (AuNPs) and random nanofibers of polyvinylidene fluoride (PVDF) by electrospinning. The structure and chemical properties of the nanofiber mat were investigated in detail by ESEM, TEM, AFM, XPS, FTIR, XRD, TGA, PL spectroscopy and UV-Vis reflectance spectra. Imaging of the composite map confirmed that the fiber diameter was in the range of 100-400 nm with the g-C_3N_4 size in the range of 2-8 μm. Backscattered (Z-contrast) electron imaging in ESEM revealed that the AuNP particle size is in the range of 60-160 nm with Au content 0.02%. XPS and FTIR recognized the chemical identify of individual components and it was revealed that chemical structure of those components remained unaltered. PL spectroscopic results revealed slight PL quenching caused by the relaxation of charge carriers in the AuNPs. Bandgap energy, as calculated by Kubeka-Munk analysis of the of the reflectance data, was found to be 2.94 eV. The photocatalytic efficiency of the nanofiber mat was confirmed by photoelectrochemical study and photocatalytic degradation of a dye, methylene blue. Methylene blue was successfully degraded by the composite mat under repeated cycles.

1. Introduction

A plasmonic photocatalyst is a special type of photocatalyst in which nanoparticles of a few selected metals are embedded onto dielectric or semiconductor materials, where the size the of the nanoparticles is less than the wavelengths of visible light. [1,2] Incidence of visible light causes localized surface plasmon resonance (LSPR) on the nanoparticle surface resulting in extreme enhancement of the local electromagnetic field. [2] Such enhancement, in turn, generates highly energetic high charge carriers, often termed as 'hot' carriers, i.e., 'hot electrons' and 'hot holes'. [3,4,5] The hot electrons can be injected to the conduction band of the semiconductor, referred to as the plasmon mediated electron transfer (PMET) [6,7,8,9,10,11,12,13,14] or LSPR sensitization effect. The 'hot carriers' can also be utilized for the direct oxidation/reduction of a chemical species if it is present in contact,which is termed as chemical interface damping (CID). [15,16,17] The hot electrons that were transferred to the conduction band of semiconductor may be directly used for a chemical reaction or transferred to different defect sites causing photoluminescent quenching thereby slowing their recombination. If the semiconductor itself can be excited by visible light as well (like for carbon nitride), then the holes from its valence band can also be transferred to the metallic nanoparticle. According to current studies, only a few selected metals, including gold (Au), silver (Ag), platinum (Pt), rhodium (Rh) and copper (Cu) have demonstrated plasmonic effects. [1,2]

Graphitic carbon nitride (C_3N_4) is one of the highly studied photocatalysts that can be excited under visible light. [18,19,20] Its facile and inexpensive synthesis method includes simple heating of 'melon' types of organic molecules, like dicyandiamide, melamine or triazine in air. It is chemically very inert and stable in acid, alkali and organic solvents thereby rendering it as a robust material as photocatalyst. Furthermore, it is also stable in air up to 600°C. [21] The first use of carbon nitride as a photocatalyst to generate hydrogen was reported in [22] 2009. After that, there was a potential shift in research from inorganic

* Corresponding author.
E-mail address: dsaha@widener.edu (D. Saha).

https://doi.org/10.1016/j.surfin.2021.101367
Received 31 January 2021; Received in revised form 21 July 2021; Accepted 22 July 2021
Available online 30 July 2021

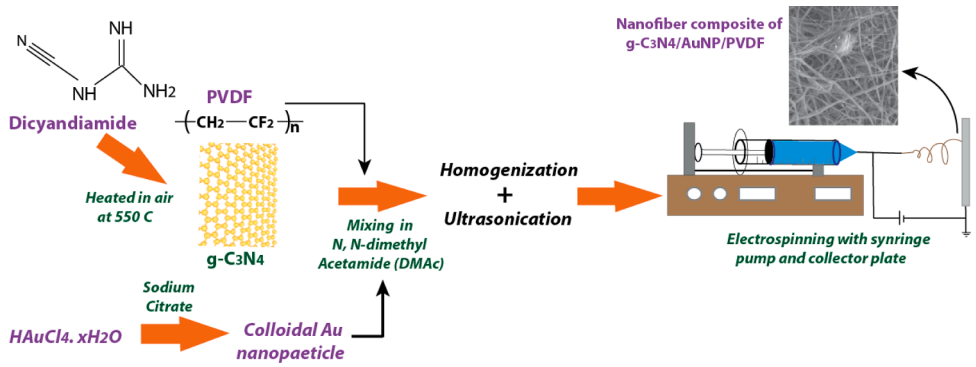

Fig. 1. Schematic of synthesis of electrospun nanofiber composite.

photocatalysts to organic and polymeric photocatalysts. [23,24] In our past research, we have demonstrated the successful role of g-C_3N_4 in dissociating different types of environmental pollutants in aqueous medium. [25,26,27,28] Owing to the few obstacles present in the practical use of carbon nitride, like low electrical conductivity, high recombination rate and limited photon absorption in the visible spectrum, different types of modifications have been suggested. In this research, we have incorporated nanoparticles of gold (AuNP) within the matrix of carbon nitride to fabricate a composite plasmonic photocatalyst.

Despite a large pool of publications reported the activity of plasmonic photocatalysts in different fields, all such reports used a bulk form of plasmonic photocatalyst. In this work, we reported the electrospun nanofibers of composite plasmonic photocatalyst consisting of AuNP/g-C_3N_4 as the active photocatalytic agent along with polyvinylidene fluoride (PVDF) as supporting nanofiber. There is a distinct advantage of using nanofiber-based composite photocatalyst in liquid medium compared to that of a bulk form. It is nearly impossible to efficiently recover bulk and powdered photocatalyst after each use in a liquid medium, while it is a very simple to recover the nanofiber mat of a photocatalyst and reuse it in multiple cycles. Owing to such benefit, the nanofiber mat would eliminate the need of new photocatalyst in every batch of reaction, which will lower the overall cost of the photocatalysis process. [29]

2. Experimental

2.1. Fabrication of nanofiber composite

Synthesis of g-C_3N_4

The synthesis of pristine carbon nitride is very similar to that of our previous reports. [25,26,27,28] Typically, 5 g dicyandiamide was put in a porcelain boat and the boat was inserted a Lindberg-Blue^{TM} tube furnace. The furnace was heated to 550°C in air within the time period of 4 hours. After that, it is cooled in air, the boat was taken out and the obtained yellow-colored g-C_3N_4 was ground in a mortar and pestle.

Synthesis of gold nanoparticles (AuNP)

In order to synthesize the gold nanoparticles (AuNP), $HAuCl_4 \bullet 3H_2O$ was used as a precursor and tribasic sodium citrate were used as reduction and capping agent. Typically, 0.088 g of $HAuCl_4 \bullet 3H_2O$ was added into 150 mL of boiling DI water within a beaker followed by addition of 1.13 g of sodium citrate onto it under constant stirring. Very soon, the color of the suspension turned from light blue to dark blue owing to the presence of plasmonic AuNPs. The suspension was continually stirred for an additional 10 minutes and then separated from heating.

Fabrication of nanofiber composite

The fabrication technique of nanofiber composite was obtained from our previous work [29] with some modifications. At first, 1.12 g of g-C_3N_4 was added in the AuNP suspension in a beaker. The water was boiled off under vigorous stirring to form an almost homogeneous and light bluish colored solid mixture of g-C_3N_4 and AuNP. The solid mass was scraped out from the beaker.

In order to fabricate the electrospun nanofiber, at first, 10 % (w/v) solution of polyvinylidene fluoride (PVDF, M_W=534,000) was made in N, N-dimethyl acetamide (DMAc). 1.5 mL of this solution along with 0.1 g of AuNP/g-C_3N_4 composite was inserted into the 2 mL tube containing zirconia beads of size 1.5 mm. Two of such tubes were loaded onto the Beadbug^{TM}-3 homogenizer (Benchmark) and shaken in 180 rpm for 3 minutes. After that, the tubes were taken out and ultrasonicated for 1 hour. The cycle of homogenization and ultrasonication was performed 5 times. After that, the homogenized slurry within the tubes were transferred to the syringe fitted with an 18 gauge needle through a luer tube. The electrospinning of this slurry was performed at the voltage of 20 kV onto a static plate with a 10-cm distance between the needle and plate. The suspension discharge rate was maintained at 1.5 mL/hr with the help of a syringe pump (SyringeONE, New Era Instrument). The schematic of fabrication of the composite nanofiber mat is shown in Fig. 1. The composite nanofiber was peeled off from the collector plate and dried in air at 50°C. For photocatalysis experiments, the nanofiber mat was sandwiched between two Teflon sheets with a cut-out window (2 cm × 2 cm) to expose the mat surface from both sides. The schematic of such assembly was shown in figure S3 of the Supplementary Material.

2.2. Characterization of nanofiber composite

Scanning electron microscope (SEM) images were obtained in two different SEMs, (a) FEI Quanta 600 FEG Mark II Environmental Scanning Electron Microscope (ESEM) and (b) FEI Quanta 400 Environmental electron microscope. Both secondary electron (SE) and backscattered electron (Z-contrast) SEM images were obtained in those microscopes. Transmission electron microscope images were obtained with an FEI Tecnai T12T Transmission electron microscope (TEM). For TEM, two types of sample preparation techniques were employed. The nanofiber mat was dispersed in isopropyl alcohol (IPA) and drop casted on a holey carbon grid for imaging. In order to better observe the AuNPs, the g-C_3N_4/AuNP composite was suspended in acetone followed by ultrasonication and drop casting on a holey carbon grid. The atomic force microscopy (AFM) images were acquired in tapping mode of AFM (i.e. amplitude modulation, AM-AFM) using an Asylum Research MFP3D system equipped with ARC2 controller. The cantilever was calibrated using silicon wafers before the measurements. The cantilever used is an AC240-TS model made by Olympus with spring constant of 2.2 N/m and resonance frequency of 69 kHz. The X-ray photoelectron (XPS) measurements were performed in Thermo K-alpha instrument (Thermo Fisher) with a monochromated Al *K*α Source (1486.7 eV) and overall 0.7 eV resolution. The charge compensation was performed by using low energy electrons and ions.

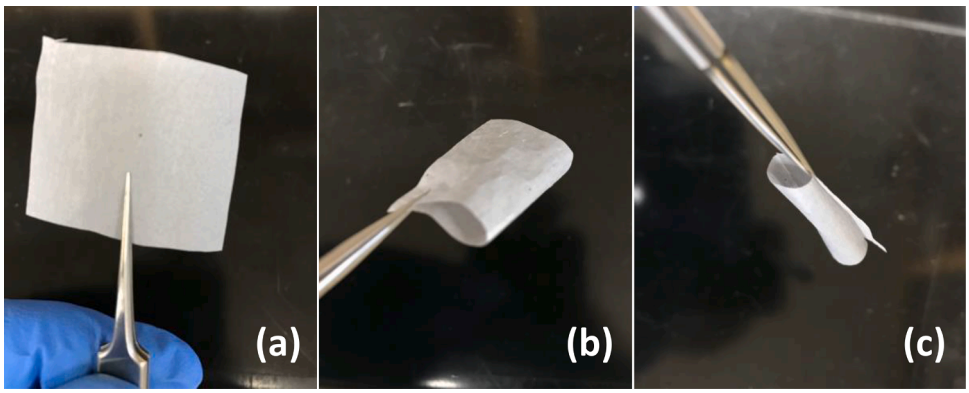

Fig. 2. Pictures of electrospun nanofiber mat.

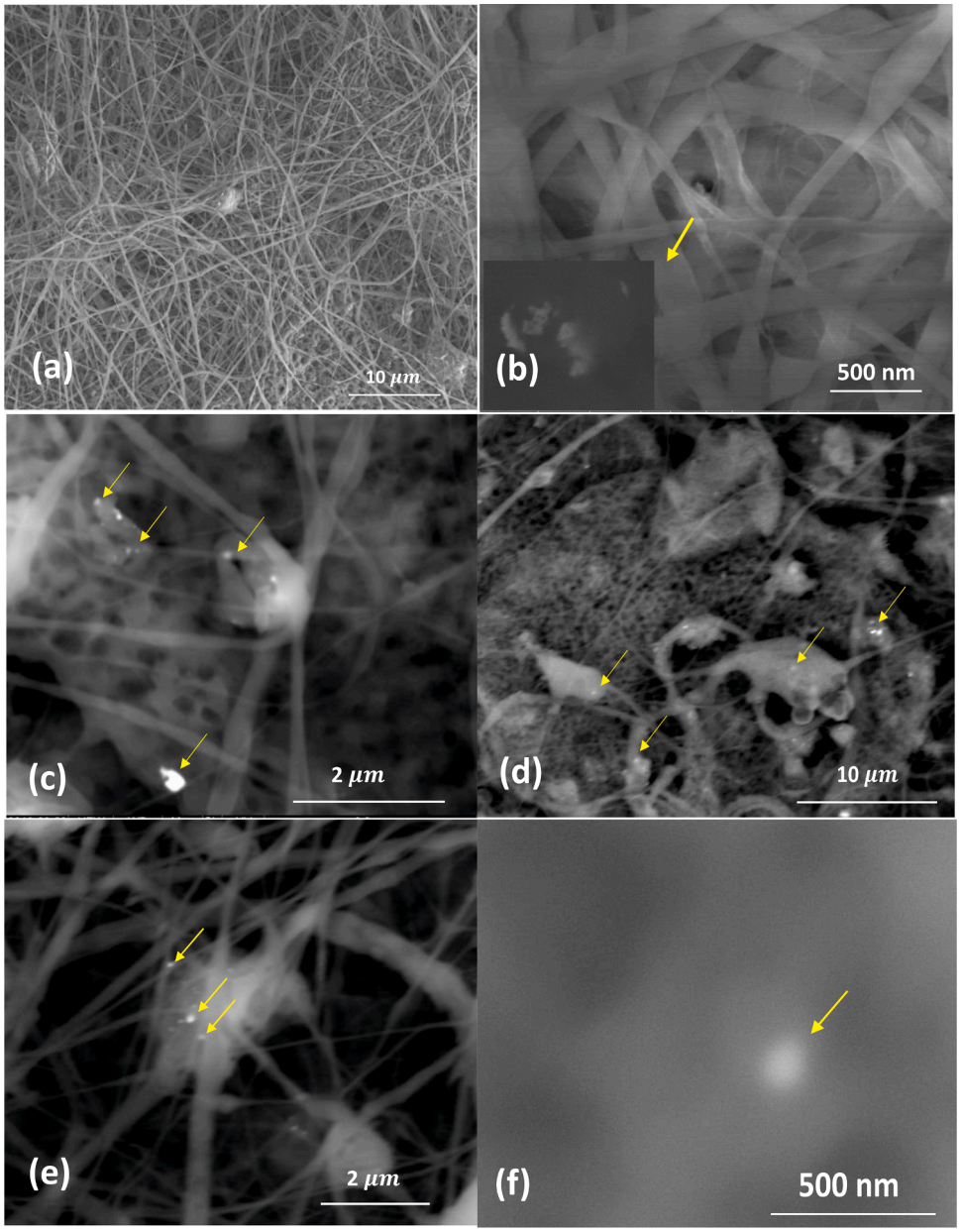

Fig. 3. Scanning Electron Microscope (SEM) images of electrospun nanofiber composite. Yellow arrows show indicate the AuNPs.

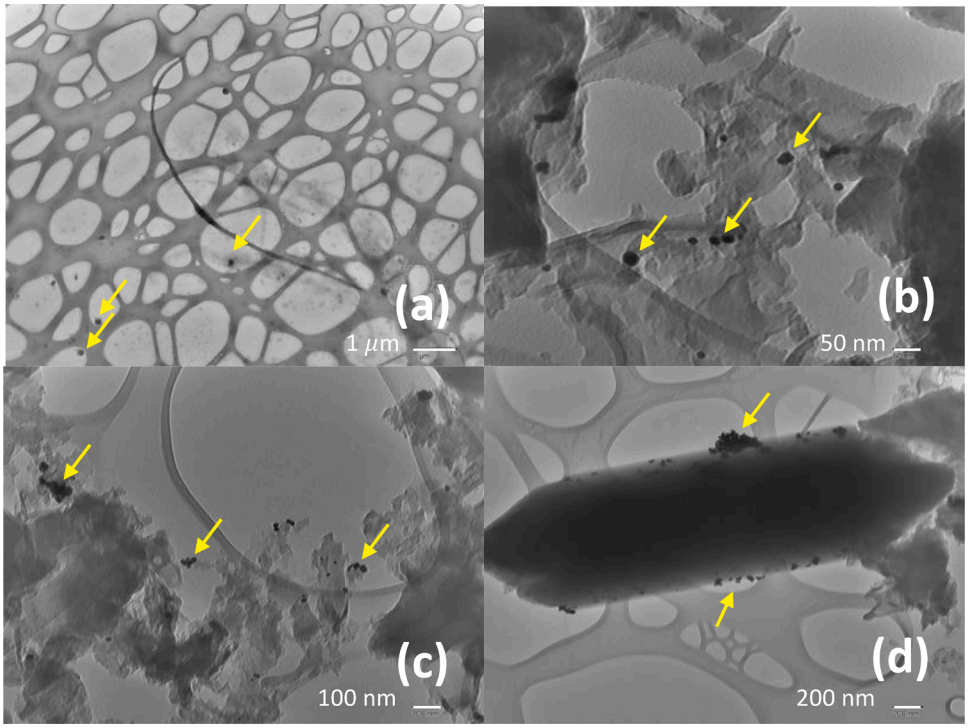

Fig. 4. Transmission electron microscope (TEM) images of electrospun nanofiber composite. Yellow arrows show indicate the AuNPs.

Photoluminescence (PL) spectroscopic data were obtained in Craic 20/30 PV Microspectrophotometer. The samples were excited at 420 nm wavelength by a Hg lamp and the emission spectra was recorded above 400 nm. The X-ray diffraction (XRD) experiments were obtained in Bruker D8 model A25 with *CuK*α as x-ray source. Scan size was 0.05°C with dwell time 1 s per step. Fourier transform Infrared (FTIR) was obtained in PerkinElmer FT-IR Spectrometer in ATR mode. The UV-Vis reflectance of the nanofiber mat was analyzed in Cary 300 Bio UV/Vis spectrometer (Agilent). UV-Vis absorption spectra of the Au/g-C_3N_4 composite was performed in Genesys UV-Vis spectrophotometer by dispersing the composite in the aqueous medium. Thermogravimetric analysis (TGA) was obtained in TA instrument's DSC Q600 SDT instrument with heating rate 10°C/min.

2.3. Photocatalysis study

2.3.1. Photoelectrochemical study

All the photoelectrochemical tests were performed with a Palm Sens3 potentiostat using platinum as counter electrode and Ag/AgCl as reference electrode (with KCl as electrolyte). The photoelectrochemical experiments were performed with both a pure nanofiber mat and the composite of g-C_3N_4/AuNP as working electrodes. The fabrication procedure of working electrode with g-C_3N_4/AuNP composite is similar to that of our previous research. [25,26] Typically, 0.012 g g-C_3N_4/AuNP complex, 60 μL DI water and 10 μL PEDOT-PSS (3-4%) were mixed in a mortar and pestle and the mixture was drop casted on a strip of indium tin oxide (ITO) coated polyethylene terephthalate (PET) film (Sigma-Aldrich) and spread by a glass rod. The assembly was annealed by heating it at 156°C in air at 10°C/min in the tube furnace. No other changes were made when the nanofiber mat was employed as the working electrode. The working electrode, reference electrode and counter electrode were positioned in a triangular fashion and inserted in a beaker with 1 M KCl solution as electrolyte. This apparatus was inserted in the same photostation where the photocatalysis experiments were carried out. All the photocatalysis experiments were performed with full intensity of light.

2.3.2. Photocatalytic decomposition

The photocatalytic decomposition experiments were performed with the methylene blue as the model pollutant. All the photocatalysis studies were performed within the 3D printed photostation fitted with two chips-on-board (COB) light emitting diodes (LEDs). For kinetic studies, 2 cassettes of composite photocatalyst were inserted in 134 mL 10 ppm methylene blue (MB) solution. It was first stirred under darkness for 30 minutes and then under full intensity of light for 2 hours. The concentration of MB was determined before the dark trial, after dark trial and within the time interval of 15 mins, 30 mins, 1 hour, 90 mins and 2 hours under light. The concentration was measured in a Genesys 10S UV-Vis spectrometer against a pre-calibrated plot. For a number of photocatalyst cassette variation study, 1, 2 and 3 cassettes were used with the same concentration of MB solution and photocatalysis was performed for 2 hours. All the runs were performed twice and the average value was reported along with standard deviation as error bars. For the cyclability study, 10 ppm of methylene blue solution was photocatalyzed in presence of two photocatalyst cassettes and within the time period of 1 hour. The residual concentration of methylene blue was measured in the same fashion. The picture of photo station and schematic of photocatalysis reaction unit has been shown in the inset of figure S1-S3 of the Supplementary Material.

3. Results and discussion

3.1. Material characteristics

The photographs of nanofiber mat are shown in Fig. 2(a-c). Although not very clear in the figure, the fiber mat has a light blue tone due to the presence of plasmonic Au nanoparticles. As observed in the figure, the fiber mat is very flexible. It can be folded or rolled without a loss of structural integrity.

SEM images captured by the FEI Quanta 600 FEG Mark II ESEM are shown in Fig. 3(a) and (b). SEM images acquired with the FEI Quanta 400 ESEM are shown in Fig. 3(c-f). As observed in Fig. 3(a-b) (Secondary electron images), there is a random network of nanofibers of diameter around 100-400 nm. It should be noted that the fiber size is not very

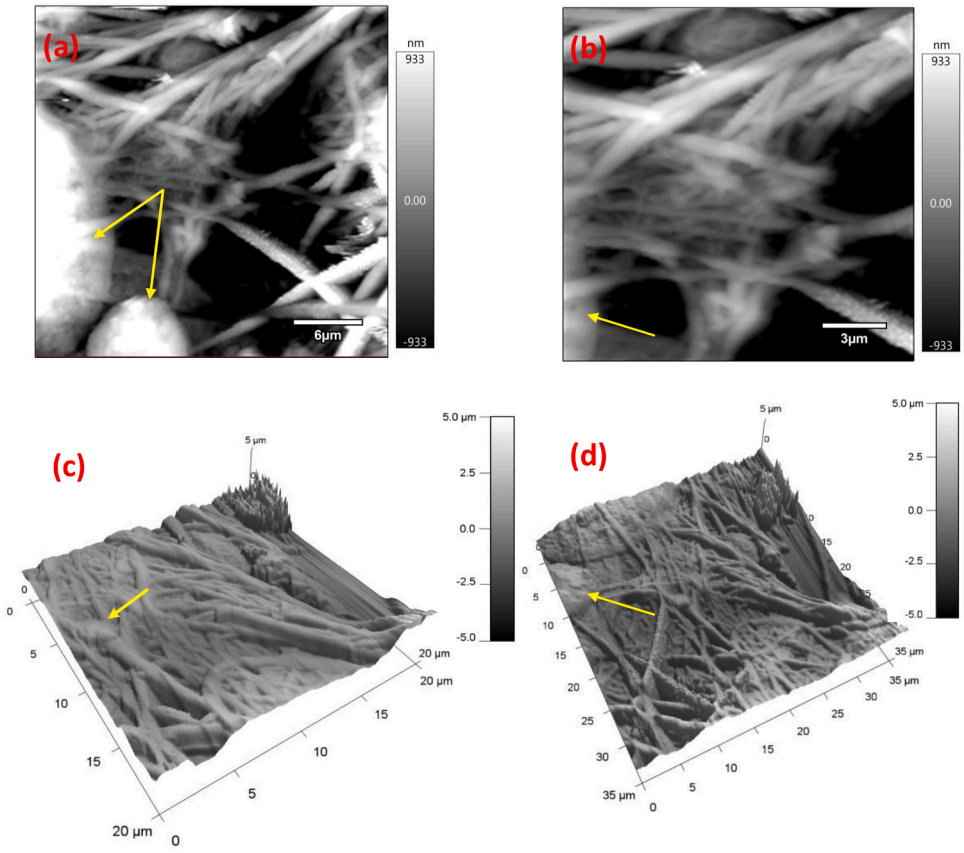

Fig. 5. Atomic force microscope (AFM) images of the nanofiber mat. Yellow arrows show indicate the g-C_3N_4 particles.

uniform compared to that of other nanofibers composed of a homogeneous polymetric system. However, our system is not homogeneous, it is highly heterogeneous. In the solution phase, we have PVDF in DMAc whereas g-C_3N_4 is dispersed in the solution in the form of micron-sized particles along with AuNPs. It is highly unlikely to have a uniform sized fiber in a such a heterogenous system. The size of g-C_3N_4 particles is around 2-8 μ*m*. In Fig. 3(b), the mode was changed from secondary electron to Z-contrast and the resultant image captured the AuNPs

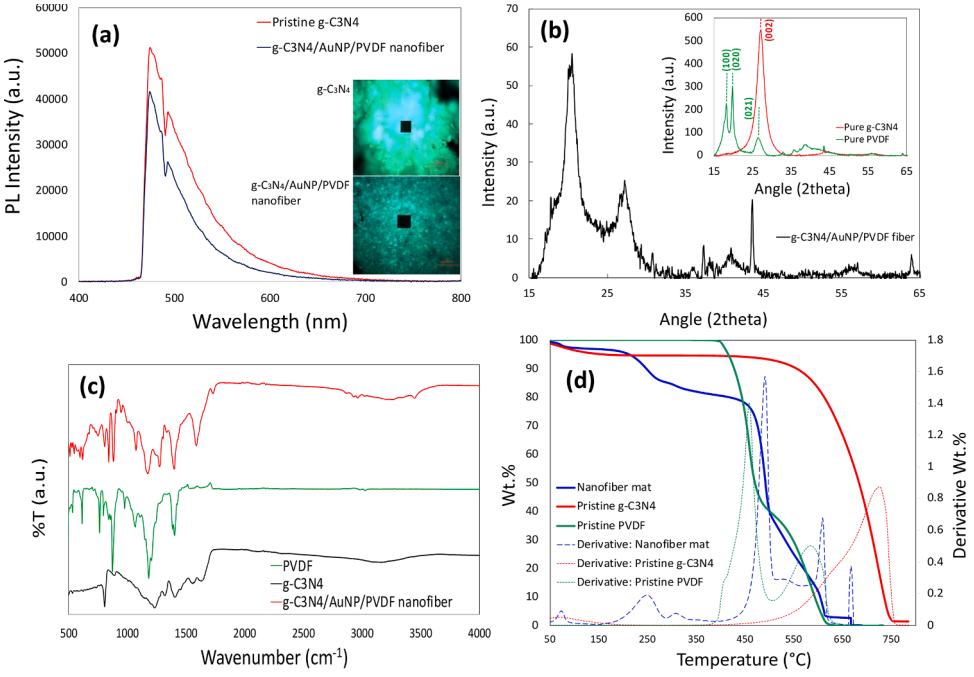

Fig. 6. Photoluminescence spectra (a) (The inset pictures show the illuminated samples upon excitation as observed under microscope.), X-ray diffraction (XRD) (b), Fourier transform infrared spectra (FTIR) (c), and Thermogravimetric analysis (TGA) (d).

shown in the inset (left bottom) of the same figure. The locations of the nanoparticles within the nanofiber assembly were marked with yellow arrows. The images shown in the Fig. 3(c-e) were obtained in the backscattered electron mode with the FEI Quanta 400 ESEM. It is clearly observed that AuNPs were expressed as bright entities (dots) within the dark contrast of nanofiber composite. In those figures, the yellow arrows were employed to properly locate the nanoparticles. The AuNPs were positioned on both g-C_3N_4 particles and the PVDF nanofiber. In the majority of cases, the nanoparticle is isolated in a discrete fashion, in a few instances, a cluster or larger agglomerate of nanoparticles was observed (bottom arrow of Fig. 3(c)). It also appears that a substantial fraction of the nanoparticles may be on the surface of the polymer rather than embedded in it. The size of the AuNPs is in the range of 60-160 nm. Fig. 3(f) shows the secondary electron image of a single AuNP of size around 65 nm. The EDX analysis of the SEM confirmed that the Au content of the sample is around 0.02 atom %.

In order to properly visualize the AuNPs, TEM images were also obtained (Fig. 4(a-d)). In the TEM images, the nanoparticles were clearly observed as dark spots and they are also designated with the yellow arrow. The first image (Fig. 4(a)) shows a TEM image where the whole nanofiber assembly was dispersed in isopropyl alcohol (IPA) and observed under TEM. The remaining images (Fig. 4(b-d)) were obtained by directly dispersing AuNP/g-C_3N_4 composites in acetone. In all the TEM images, the nanoparticles were clearly observed as dark spots and their location in indicated by the yellow arrows. In Fig. 4(d), it is observed that the AuNPs were anchored on a g-C_3N_4 particle where both individual and clusters of nanoparticles are present. Atomic force microscopic (AFM) images are shown in Fig. 5(a-d). Fig. 5(a-b) show the 2D scans whereas 5(c) and (d) show the 3D topographical images. The 2D scans demonstrate the nanofiber assemblies and g-C_3N_4 particles, similar to that of SEM images. The 3D topographical images reveal the surface roughness caused by the random network nanofiber assembly and g-C_3N_4 particles. The g-C_3N_4 particles are indicted by yellow arrows.

A photoluminescence (PL) spectrum of a g-C_3N_4/AuNP/PVDF nanofiber mat is shown in Fig. 6(a) along with that of pristine g-C_3N_4 for comparison. It appears that the PL peak intensity of composite nanofiber mat is slightly lower than that of pristine g-C_3N_4. The PL intensity is caused by the radiative recombination of charge carriers, i.e., electrons and holes when they recombine. The reduction of PL intensity or PL quenching usually signifies the reduced rate of radiative recombination and, hence, their higher availability in a chemical reaction. In the nanofiber mat, the PL quenching is most likely caused by the relaxation of the charge carriers onto the AuNPs thereby slightly increasing the life span. The X-ray diffraction (XRD) patterns of nanofiber mat are shown in Fig. 6(b) along with XRD or pristine g-C_3N_4 and PVDF in the inset. The key peak of pristine g-C_3N_4 is located at 27°, which is associated with the (002) reflection. Pure PVDF is also crystalline with prominent peaks at 18.2°, 19.8° and 26.4° that are associated with the (100), (020) and (021) reflection planes. These peaks suggest that the PVDF is in it α pahse. The XRD of the nanofiber shows the prominent (020) and (002) peaks attributed to the PVDF and g-C_3N_4 along with few smaller peaks suggesting no possible change in the crystalline structures of the individual components.

Fourier transform infrared (FTIR) spectra of nanofiber mat, pristine g-C_3N_4 and pure PVDF are shown in Fig. 6(c). For pristine g-C_3N_4, the main peak is at 809 cm^{-1} that is attributed to the repeating triazine units. Several other peaks of g-C_3N_4 that are also observed in the FTIR are at 1401, 1555 and 2131 cm^{-1} that are the representatives of C-C sp [3], C=N and C-N functionalities, respectively. For pure PVDF, the main peaks are at 1410, 1180, 840, 763 and 615 cm^{-1}, that represent in-plane bending of CH_2 groups, CH_2/CH_3 deformation, rocking and asymmetric stretching of CH_2/CF_2 groups, in-plane bending of CH_2 and CF_2 groups and CF_2 and CCC skeletal vibration, respectively. In the FTIR of the nanofiber composite, majority of those peaks are still observed suggesting that there is no possible chemical change of the individual components. The thermogravimetric analysis (TGA) plot of the

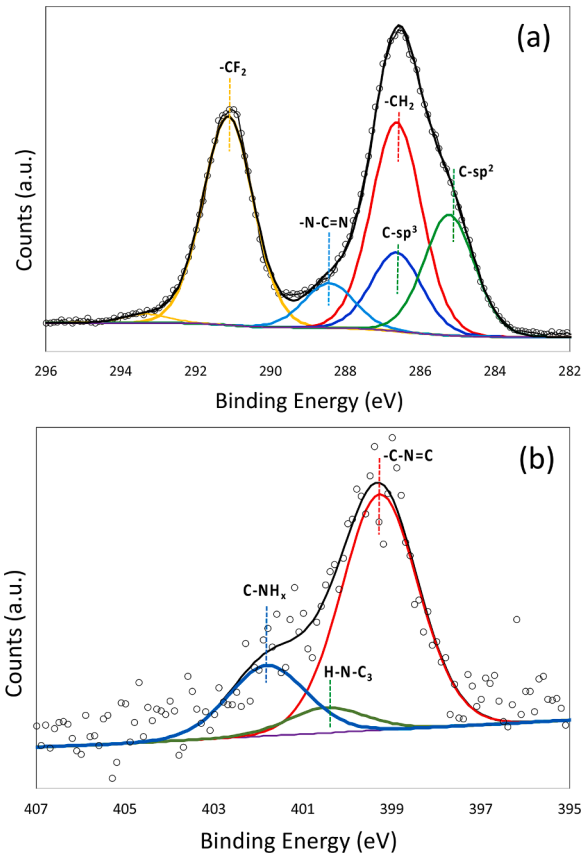

Fig. 7. XPS peak fitting of C1s (a) and N1s (b) for nanofiber mat.

nanofiber mat in air is shown in Fig. 6(d). In order to compare with the individual components, TGA of pristine PVDF and pristine g-C_3N_4 in air are also shown in the same figure. The derivative of TGA shows the key temperature of dissociation as the decomposition peaks. The thermal decomposition of PVDF and g-C_3N_4 was clearly observed in the in the derivative TGA pattern of the composite nanofiber mat. In addition, we also measured the UV-Vis absorption spectra of the Au/g-C_3N_4 composite in dispersed form in aqueous medium and they are given in figure S4 of the Supplementary Material. It shows the presence of AuNPs as a weak peak centered at around 543 nm.

The overall XPS patterns revealed the key elements as C, N, O and F with the atomic percentages of 56.63, 0.48, 2.71 and 40.18, respectively. It needs to be noted that, due to the very small atomic fraction of Au, the Au-4f peak deconvolution could not be performed with satisfactory statistics and hence was not reported. The peak fitting results of two key elements, C-1s and N-1s are shown in Fig. 7(a) and (b), respectively. In C-1s peak fitting, the large peak originated at the binding energy (BE) of 291.13 eV constitutes 17.71 at.% of total carbon and is associated with CF_2 functionalities that originated from PVDF fiber. Sp [2] and sp [3] hybridized carbons with the BE at 285.23 eV and 286.63 eV constitute around 10.17 at.% and 6.64 at.% of all the elements. These functionalities may originate from PVDF and g-C_3N_4 (as defect sites). The CH_2 functionality, that is contributed by PVDF consists of 17.66 at.%. N-C=N functionality, [30,31,32] which bears the key signature of g-C_3N_4 appears at the BE of 288.43 eV and contributes to 3.78 at.%. However, it needs to be noted that oxygen functionalities may be partially attached to the carbon of g-C_3N_4 structure, and hence contribute to the C-O (286 eV) and C=O (289 eV) functionalities. These oxygen contributions might have partially contributed to the -CH_2 and N-C=N peak fitting results. In N-1s peak deconvolution, the key functionalities are sp [2] hybridized nitrogen, [30,31,32] (C-N=C), amino nitrogen (C-NH_x) and sp [3] hybridized nitrogen (H-N-C_3), and their

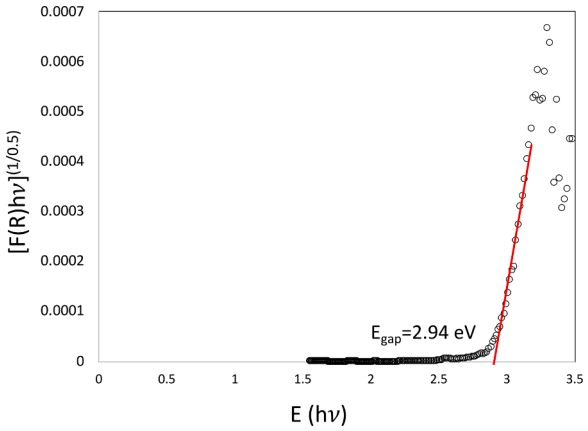

Fig. 8. Linear regression of Kubelka-Monk plot.

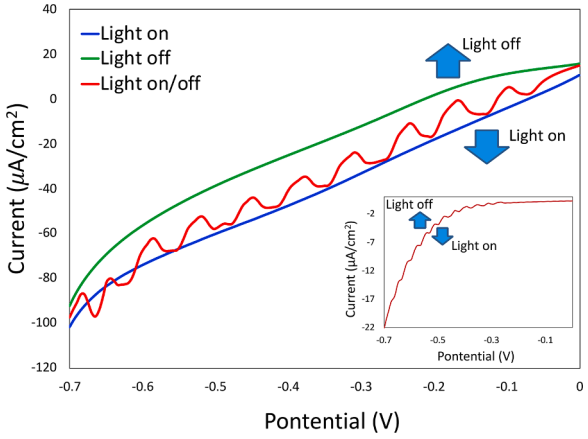

Fig. 9. Photoelectrochemical response of g-C_3N_4/AuNP composite (inset: Photoelectrochemical response of composite nanofiber mat).

atomic percentages are 0.34, 0.1 and 0.04, respectively. Among those functionalities, C-N=C is the key signature of g-C_3N_4.

The Kubeka-Munk function ($F(R)$) can be obtained from the reflectance data (R) given as [33] $F(R) = \frac{\alpha}{s} = \frac{(1-R)^2}{2R}$ …(1). Where, α is the reflectivity and s is the scattering factor. Since the scattering factor is independent of wavelength, the Kubelka-Munk function is proportional to the absorptivity. McLean analysis [34] of the absorption edge can be applied to the reflection data to find the optical badgap (E_g) as $F(R).h\nu = k(h\nu - E_g)^{1/n}$ …..(2). With n=2 for direct allowed transition, the bandgap energy (E_g) can be calculated by the linear regression of $F(R)h\nu^2$ versus $h\nu$ plot. The regression plot is shown in Fig. 8 with a calculated bandgap energy of 2.94 eV.

3.2. Photocatalysis studies

3.2.1. Photoelectrochemical studies

Photoelectrochemical responses of the photocatalyst is shown in Fig. 9. The inset of the figure shows the response of the actual nanofiber mat with the intermittent light (i.e., light on/off). Despite the changes in the current response, the intermittent light is clearly visible in the plot, the response current was not observed to be strong. It is probably caused by the large amount of nonconducting PVDF fiber in the system that did not allow the photogenerated charge carriers to flow through to the system and reach the sensor of potentiostat. In order to further analyze the response, we have directly deposited the g-C_3N_4/AuNP composite onto an ITO coated PET film (see experimental section 2.3). The photoelectrochemical response of such films are shown in Fig. 9. This figure

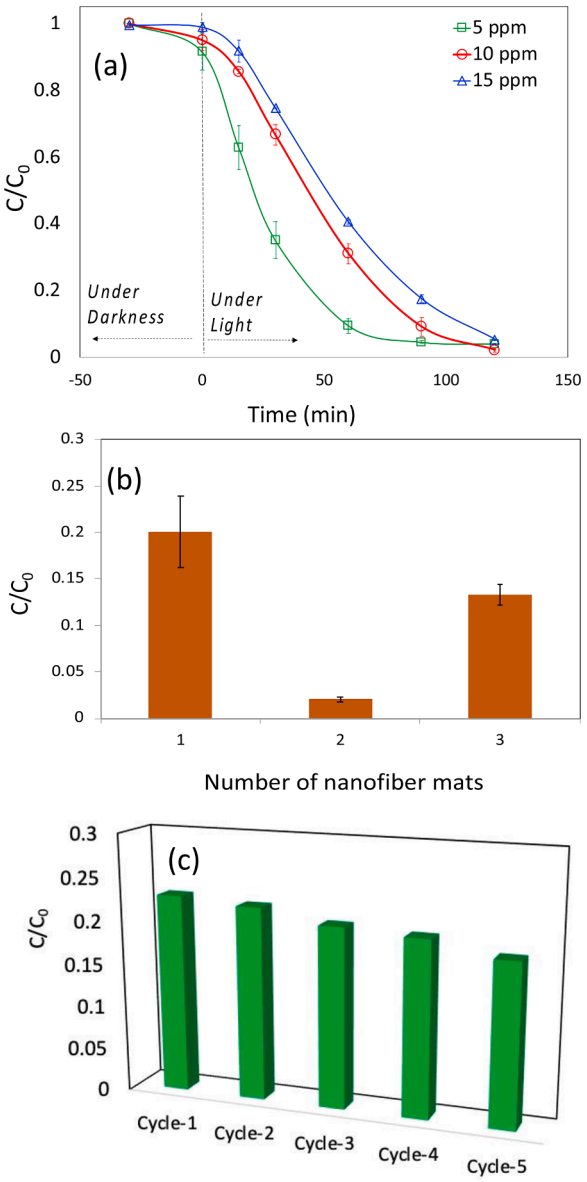

Fig. 10. Kinetics of photocatalytic decomposition of methylene blue (MB) (a), influence of number of nanofiber mat in decomposing MB (b), cyclability of photocatalysis of MB (c).

clearly shows that changes in the photocurrent with the incident light and with the intermittent light variation.

3.2.2. Photocatalytic decomposition

The kinetics of photocatalytic degradation of methylene blue (MB) is shown in Fig. 10 (a). As observed in the figure, a small amount of MB disappeared under darkness that is attributed to the adsorption of the MB on the surface of nanofiber composite. Upon exposure to the full intensity of light, MB immediately started to decompose and almost completely degraded within two hours. As expected, within three initial concentrations of 5, 10 and 15 ppm of MB, 5 ppm MB degraded faster followed by 10 and 15 ppm. The details of the reaction mechanism of photocatalytic degradation of MB were investigated in detail in our previous publication. [28] Initially, the MB molecule undergoes de-chlorination and demethylation to form another dye, Azure B. These molecules eventually undergo ring opening reactions to form smaller straight chain molecules. [28] It needs to be noted that methylene blue may undergo partial self-oxidation under light; however, according to our previous study, the self-oxidation of methylene blue under the same

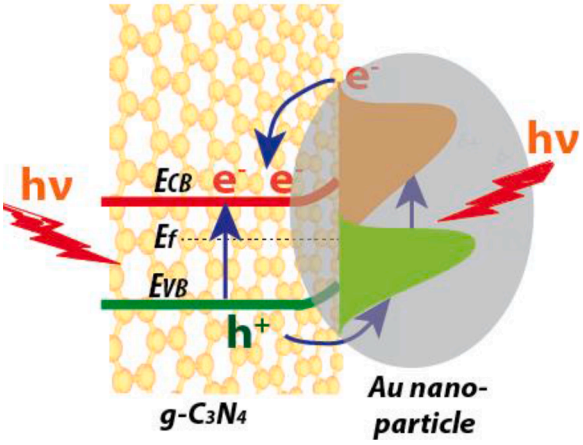

Fig. 11. Schematic of plasmonic photocatalysis.

light is negligible, not more than 1-2% [28].

The influence of the number of fiber mats is shown in Fig. 10(b). It is observed that the degree of photocatalysis increased with the increase in the number of fiber mats from 1 to 2; however, it decreased with further increase of mats to 3. Such atypical behavior of photocatalysis was also observed in our previous publication, [29] and this can be attributed to a similar reason. With the initial increase in number of fiber mats from 1 to 2, the degree of photocatalytic degradation of MB increased owing to an increase in amount of photocatalyst in the system. However, when the number of fiber mat was further increased to 3, it caused crowding of the mats in the beaker that potentially inhibited the number of photons (light) in the system. Such a situation lowered the effective photocatalysis of MB. We could not further increase the number of mats in the system as there was no space available in the reacting medium to insert another fiber. Furthermore, it is also quite intuitive to hypothesize that the influence of the number of fiber mats strongly depends on the geometry of the reaction medium; a larger medium would have accommodated a larger number of fiber mats without inhibiting the number of incident photons. The cyclability of photocatalytic decomposition of MB is shown in Fig. 10 (c). It was observed that a nanofiber mat can well maintain the similar photocatalytic degradation of MB after 5 cycles. It needs to be noted that while the static surface charge may also influence the degradation of the methylene blue, it can be well argued that charge carriers generated on the surface of photocatalyst mat in the course of the photocatalysis are the true species that degraded methylene blue. This conclusion can be further verified from the fact that degradation of methylene blue under darkness was negligible compared to that of under light.

The general working principle of a plasmonic photocatalyst is mentioned in the introduction section. Incidence of visible light on AuNPs introduces localized surface plasmon resonance (LSPR) effect causing the generation of energetically high charge carriers, i.e., electrons and holes. Energetically high electrons are injected from AuNPs onto the conduction band of g-C_3N_4. These electrons along with the other charge carriers generated in the conduction and valence bands of g-C_3N_4 are utilized in the chemical reaction of the photocatalysis process. In addition, the holes generated in the valence band of the g-C_3N_4 may also be transferred to the valence band of AuNPs causing a charge separation and better availability of charge carriers in the course of photocatalysis. The overall schematic of photocatalysis is shown in Fig. 11.

4. Conclusion

In this work, we have successfully fabricated a plasmonic composite nanofiber mat of g-C_3N_4/AuNP in a matrix of random PVDF nanofibers. The morphology of the composite mat was investigated in detail by secondary and backscattered electrons in ESEM, TEM and AFM. It was revealed that the fiber diameter was in the range of 100-400 nm, whereas the particle size of g-C_3N_4 was in the range of 2-8 μm. ESEM imaging in backscattered electron mode found that AuNP size was in the range of 60-160 nm with 0.02% Au. The chemical identity of the individual components was confirmed by FTIR and XPS, and it was observed that individual components retained their identity in the composite. PL spectroscopic results revealed a small PL quenching that might have been caused by relaxation of charge carriers within the AuNP. Kubelka-Monk Analysis of the reflectance spectra revealed the bandgap energy of the composite mat is 2.94 eV. The photoelectrochemical studies and photocatalytic degradation of methylene blue under repeated cycles by the nanofiber composite confirmed its successful role as a photocatalyst.

Declaration of Competing Interest

The authors declare that they have no known competing financial interests or personal relationships that could have appeared to influence the work reported in this paper.

Acknowledgement

This work has been financially supported by School of Engineering (SOE) of Widener University. This work was also partially supported by 2018 Water Resources Research projects USGS 104B, Pennsylvania. D.S. acknowledges the faculty development award from Widener University. Photoluminescence (PL) spectroscopy was performed in part at the Chapel Hill Analytical and Nanofabrication Laboratory, CHANL, a member of the North Carolina Research Triangle Nanotechnology Network, RTNN, which is supported by the National Science Foundation, Grant ECCS-1542015, as part of the National Nanotechnology Coordinated Infrastructure, NNCI. Support for KWK and SLS was provided by National Science Foundation award #1825331 and the facilities of the Center for Microanalysis and Imaging Research and Training (CMIRT) at West Chester University.

Supplementary materials

Supplementary material associated with this article can be found, in the online version, at doi:10.1016/j.surfin.2021.101367.

References

[1] Y. Zhang, S. He, W. Guo, Y. Hu, J. Huang, J.R. Mulcahy, W.D. Wei, Surface-Plasmon-Driven Hot Electron Photochemistry, Chem. Rev. 118 (2018) 2927–2954..
[2] X. Zhang, Y.L. Chen, R-S. Liu, D.P. Tsai, Plasmonic photocatalysis, Rep. Prog. Phys. 76 (2013), 046401..
[3] M.L. Brongersma, N.J. Halas, P. Nordlander, Plasmon-Induced Hot Carrier Science and Technology, Nat. Nanotechnol. 10 (2015) 25–34..
[4] J.B. Khurgin, How to Deal with the Loss in Plasmonics and Metamaterials, Nat. Nanotechnol. 10 (2015) 2–6..
[5] D.D. Ryutov, Landau Damping: Half a Century with the Great Discovery. Plasma Phys, Controlled Fusion 41 (1999) A1–A12..
[6] S. Linic, P. Christopher, D.B. Ingram, Plasmonic-Metal Nanostructures for Efficient Conversion of Solar to Chemical Energy, Nat. Mater. 10 (2011) 911–921..
[7] J.S. DuChene, B.C. Sweeny, A.C. Johnston-Peck, D. Su, E.A. Stach, W.D. Wei, Prolonged Hot Electron Dynamics in Plasmonic-Metal/Semiconductor Heterostructures with Implications for Solar Photocatalysis, Angew. Chem., Int. Ed. 53 (2014) 7887–7891..
[8] S. Hung, F. Xiao, Y. Hsu, N. Suen, H.M.Chen Yang, B. Liu, Iridium Oxide-Assisted Plasmon-Induced Hot Carriers: Improvement on Kinetics and Thermodynamics of Hot Carriers, Adv. Eng. Mater. 6 (2016), 1501339..
[9] K. Qian, B.C. Sweeny, A.C. Johnston-Peck, W. Niu, J.O. Graham, J.S. DuChene, J. Qiu, Y. Wang, M.H. Engelhard, D. Su, E.A. Stach, W.D. Wei, Surface Plasmon-Driven Water Reduction: Gold Nanoparticle Size Matters, J. Am. Chem. Soc. 136 (2014) 9842–9845..
[10] M.W. Knight, H. Sobhani, P. Nordlander, N.J. Halas, Photodetection with Active Optical Antennas, Science 332 (2011) 702–704..
[11] C. Clavero, Plasmon-Induced Hot-Electron Generation at Nanoparticle/Metal-Oxide Interfaces for Photovoltaic and Photocatalytic Devices, Nat. Photonics 8 (2014) 95–103..

[12] Y. Tian, T. Tatsuma, Plasmon-Induced Photoelectrochemistry at Metal Nanoparticles Supported on Nanoporous TiO_2, Chem. Commun. (2004) 1810–1811..
[13] S.C. Warren, E. Thimsen, Plasmonic Solar Water Splitting, Energy Environ. Sci. 5 (2012) 5133–5146..
[14] S.K. Cushing, N. Wu, Progress and Perspectives of Plasmon-Enhanced Solar Energy Conversion, J. Phys. Chem. Lett. 7 (2016) 666–675..
[15] C. Boerigter, R. Campana, M. Morabito, S. Linic, Evidence and Implications of Direct Charge Excitation as the Dominant Mechanism in Plasmon-Mediated Photocatalysis, Nat. Commun. 7 (2016) 10545..
[16] C. Boerigter, U. Aslam, S. Linic, Mechanism of Charge Transfer from Plasmonic Nanostructures to Chemically Attached Materials, ACS Nano 10 (2016) 6108–6115..
[17] B.N.J. Persson, Polarizability of Small Spherical Metal Particles: Influence of the Matrix Environment, Surf. Sci. 281 (1993) 153–162..
[18] W.-J. Ong, L.-L. Tan, Y.H. Ng, S.-T. Yong, S.-P. Chai, Graphitic Carbon Nitride (g-C_3N_4)-Based Photocatalysts for Artificial Photosynthesis and Environmental Remediation: Are We a Step Closer To Achieving Sustainability? Chem. Rev. 116 (2016) 7159–7329..
[19] Z. Zhao, Y. Sun, F. Dong, Graphitic carbon nitride based nanocomposites: a review, Nanoscale 7 (2015) 15–37.
[20] S. Cao, J. Low, J. Yu, M. Jaroniec, Polymeric Photocatalysts Based on Graphitic Carbon Nitride, Adv. Mater. 27 (2015) 2150–2176..
[21] C.H. Ao, S.C. Lee, Indoor air purification by photocatalyst TiO_2 immobilized on an activated carbon filter installed in an air cleanerChem, Eng Sci 60 (2005) 103–109..
[22] C.C Chan, J.D. Spengler, H. Özkaynak, M. Lefkopoulou, Commuter Exposures to VOCs in, 41, Air Waste Manage. Assoc., Boston, Massachusetts, 1991, pp. 1594–1600..
[23] N.J. Lawryk, C.P. Weisel, Concentrations of Volatile Organic Compounds in the Passenger Compartments of Automobiles, Environ. Sci. Technol. 30 (1996) 810–816..
[24] M. Dechow, H. Sohn, J. Steinhanses, Concentrations of selected contaminants in cabin air of airbus aircraft, Chemosphere 35 (1997) 21–31..
[25] D. Saha, M.C. Visconti, M.M. Desipio, R. Thorpe, Inactivation of Antibiotic Resistance Genes by Ternary Nanocomposites of Carbon Nitride, Reduced Graphene Oxide and Iron Oxide Under Visible Light, Chemical Engineering Journal 382 (2019), 122857, https://doi.org/10.1016/j.cej.2019.122857.
[26] M.M. Desipio, S.E. Van Bramer, R. Thorpe, D. Saha, Photocatalytic and Photo-Fenton Activity of Iron Oxide-doped Carbon Nitride in 3D Printed and LED driven Photon Concentrator, J. Hazardous Materials 376 (2019) 178–187..
[27] M.M. Desipio, R. Thorpe, D. Saha, Photocatalytic Decomposition of Paraquat Under Visible Light by Carbon Nitride and Hydrogen Peroxide, Optik 172 (2018) 1047–1056..
[28] D. Saha, M.M. Desipio, T.J. Hoinkis, E.J. Smeltz, R. Thorpe, D.K. Hensley, J.Chen S. G.Fischer-Drowos, Influence of Hydrogen Peroxide in Enhancing Photocatalytic Activity of Carbon Nitride Under Visible Light: An Insight into Reaction Intermediates, J. Environ. Chem. Eng. 6 (2018) 4927–4936..
[29] D. Saha, T.J. Hoinkis, Electrospun, Flexible and Reusable Nanofiber Mat of Graphitic Carbon Nitride for Photocatalytic Reduction of Hexavalent Chromium, J. Colloid Interface Science 575 (2020) 433–442..
[30] J-R Zhang, Y. Ma, S-Y. Wang, J. Ding, B. Gao, E. Kan, W. Hua, Accurate K-edge X-ray photoelectron and absorption spectra of g C_3N_4 nanosheets by first-principles simulations and reinterpretations, Phys. Chem. Chem. Phys. 21 (2019) 22819–22830..
[31] S.-W. Cao, X.-F. Liu, Y.-P. Yuan, Z.-Y. Zhang, Y.-S. Liao, J. Fang, S.C.J. Loo, T. C. Sum, C. Xue, Appl. Catal. B 147 (2014) 940..
[32] Z. Zhang, J. Huang, M. Zhang, L. Yuan, B. Dong, Appl. Catal. B 163 (2015) 298..
[33] P. Kubelka, F. Munk, Z. Tech. Phys. 11 (1931) 593–601..
[34] T.P. McLean, in: A.F. Gibson (Ed.), Progress Semiconduct. 5 (1960) 55–102.